

# **Magnetic Sensor Development Using Finite Element Analysis**

**T.J. Wagener, James R. Campbell, Jr., and James E. Lenz**

**Honeywell Systems and Research Center  
3660 Technology Drive, Minneapolis, MN 55418**

## **Abstract**

Magnetic finite element analysis has proven to be valuable in the research and development of magnetic sensors and actuators. The emphasis of this research is not entirely on design detail, but also on the basic magnetics and material properties on which devices are based. Examples of this research include: 1) magnetic shielding for ring-laser gyros, 2) magnetic force modeling for accelerometers based on the type-two high-temperature superconductors, 3) proximity and position sensors for aircraft applications, and 4) the dynamics of and losses in electromagnetic actuators and bearings. These examples represent the wide diversity of magnetic problems faced by researchers, and demonstrate how solutions to these problems range from simple two-dimensional models to larger and more complicated three-dimensional models.

## Introduction

Magnetic finite element analysis provides crucial design insight for both the production engineer and the research and development scientist. For production engineers, detailed magnetic finite element analysis streamlines prototype design and development and thus provides for accurate component dimensions and tolerances in a cost effective way. Furthermore, these studies provide insight into the trade-off between component performance and the ability to manufacture the components cost effectively. For the research and development scientist, magnetic finite element analysis provides for parametric design studies that verify and/or enhance new product designs and concepts.

In this paper, we present a diversity of MSC/EMAS studies that exemplify its use in both the production and the research and development environments. The first example is in the area of magnetic shielding. Work in this area ranges from determining the shielding effects for a variety of different materials under varying conditions to the details of how to shield Honeywell's ring-laser gyros. The second example discusses a new accelerometer design incorporating the high-transition temperature superconductors, and the use of non-linear magnetostatic analysis to replicate the diamagnetism of a type-two superconductor. The third example shows the use of frequency response analysis to determine optimum aircraft proximity and position sensor designs. The fourth example discusses a simple two-dimensional model that aided in the understanding of a three degree of freedom rotor/stator actuator.

## Magnetic Shielding of Ring Laser Gyros

### *Problem Definition*

There are three main categories for magnetic shielding. The first category is the shielding of high frequency electromagnetic fields, commonly accomplished by using conducting materials such as copper or aluminum. Here the attenuation is established through eddy currents generated in the conducting material. The performance is limited by the skin depth of the material,  $\delta$ , which is proportional to  $1/\sqrt{\mu f \sigma}$  where  $\mu$  is the permeability,  $f$  is the frequency, and  $\sigma$  is the electrical conductivity.

The second category for magnetic shielding is high intensity low frequency fields. The common technique for this shielding is the use of ferromagnetic materials that have very high permeabilities. In this case, the material thickness is designed such that the material operates in the linear region of the B-H curve. The performance is limited by the initial permeability and saturation of the material as well as demagnetization effects due to the shape of the shield.

The third category for magnetic shielding is low intensity low frequency fields where superconducting materials have a significant advantage.<sup>1</sup> For low intensity fields the ferromagnetic materials do not work well because it is difficult to make the material thin enough to get the material operating in the linear-range of the B-H curve without sacrificing strength that is needed to hold the high tolerances in the gaps of the magnetic shield. Superconductors are diamagnetic material with permeability much less than one. Whereas a ferromagnetic material concentrates the flux, a diamagnetic material repels magnetic flux. An advantage of a diamagnetic shield is that the effect of apertures is reduced since the flux is not concentrated across these openings.

Figure 1 shows a comparison between the three types of magnetic shields. This data was generated using finite element analysis for a geometry where the shielded material was inserted between a transmitting and receiving coil. The shield consisted of an infinitely long sheet. For a

highly conductive material (i.e. copper) the shielding attenuation is frequency dependent, as expected. The ferromagnetic material is not as frequency dependent but requires sound engineering of gaps and operating the material in the linear-range of the B-H curve. Curves for two different diamagnetic materials show that they can achieve good attenuation for good superconducting materials.

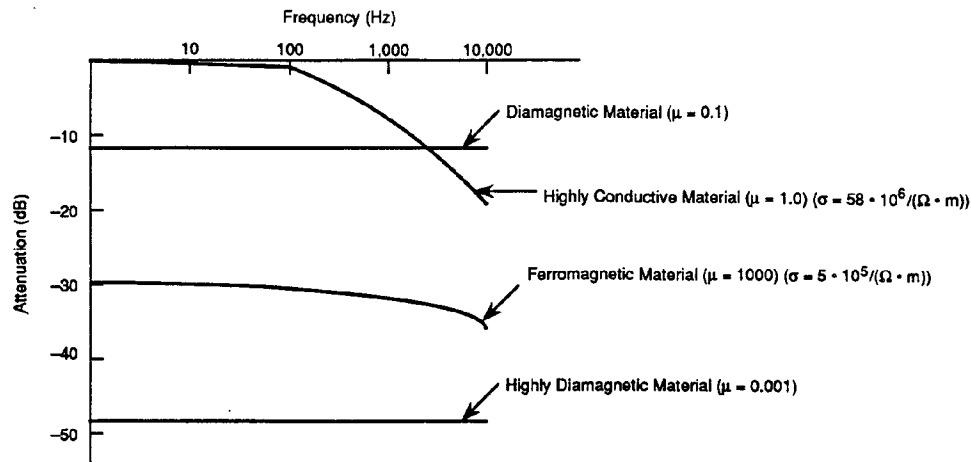


**Figure 1** Shielding attenuation vs. sample parameters ( $\mu$  and  $\sigma$ ).

A challenging shielding problem is for high sensitivity sensors because minimal size and weight increases are allowed to the sensor housing. For our Ring-Laser Gyro (RLG) a magnetic shield is needed to reduce the ambient earth's field of 0.5 Gauss by a factor of 200. A two piece, clamshell-like container was designed to conform to the RLG triangular shape and made with 0.040 inches of high permeability material (hypernom). The magnetic attenuation of this shield was predicted to be several thousand but laboratory measurements show the attenuation to be approximately 20. Finite element analysis was performed to understand this unexpected result.

### **Analysis**

A two-dimensional finite element model was generated for a RLG magnetic shield. Figure 2 shows the field line plots for two field orientations. The thin elements are hypernom and the thicker bottom piece is invar. A non-linear B-H curve was used for hypernom and a linear permeability of 1000 was used for the invar. This model predicted a magnetic attenuation of greater than 1000 inside the magnetic shield.

Since the magnetic shield consists of two parts, it is possible that an air gap is present between the two parts. To investigate this, a variable gap was added to the model along the side of the hypernom shield. Figure 3 shows the computed attenuation versus this gap spacing for the two field orientations. The effects of the air gap is clearly noticed. In fact, the finite element analysis results for a 0.001 inch gap coincides with the experimentally measured values.

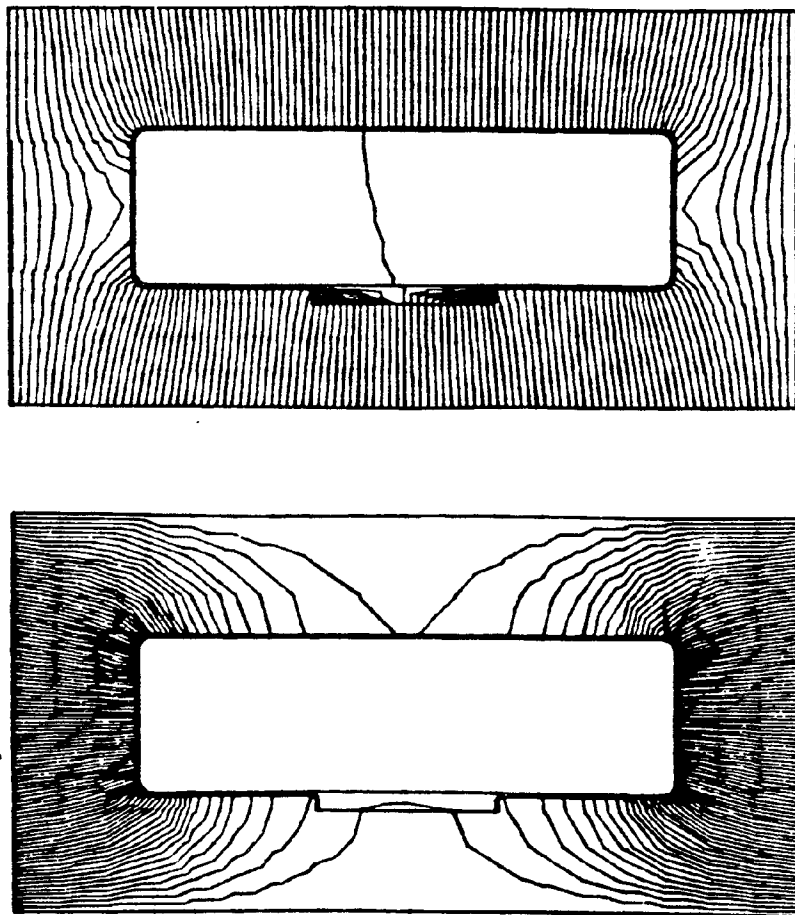


**Figure 2 Two-dimensional magnetic field line plot for two field orientations incident on RLG magnetic shield.**

### ***Discussions***

The modeling showed that to produce an effective magnetic shield it is more important to minimize the gap than to select the highest permeable material. Shields from more workable materials such as hypemik are preferred and emphasis is placed on a continuous tight fit with overlap. A second aspect of these results is that emphasis is placed on locating the holes and edges of the shield in locations that minimize the fields leaking into the most sensitive regions of the sensor. That is, the field is pushed away from the sensitive regions of the sensor rather than trying to produce a uniform zero gauss chamber.

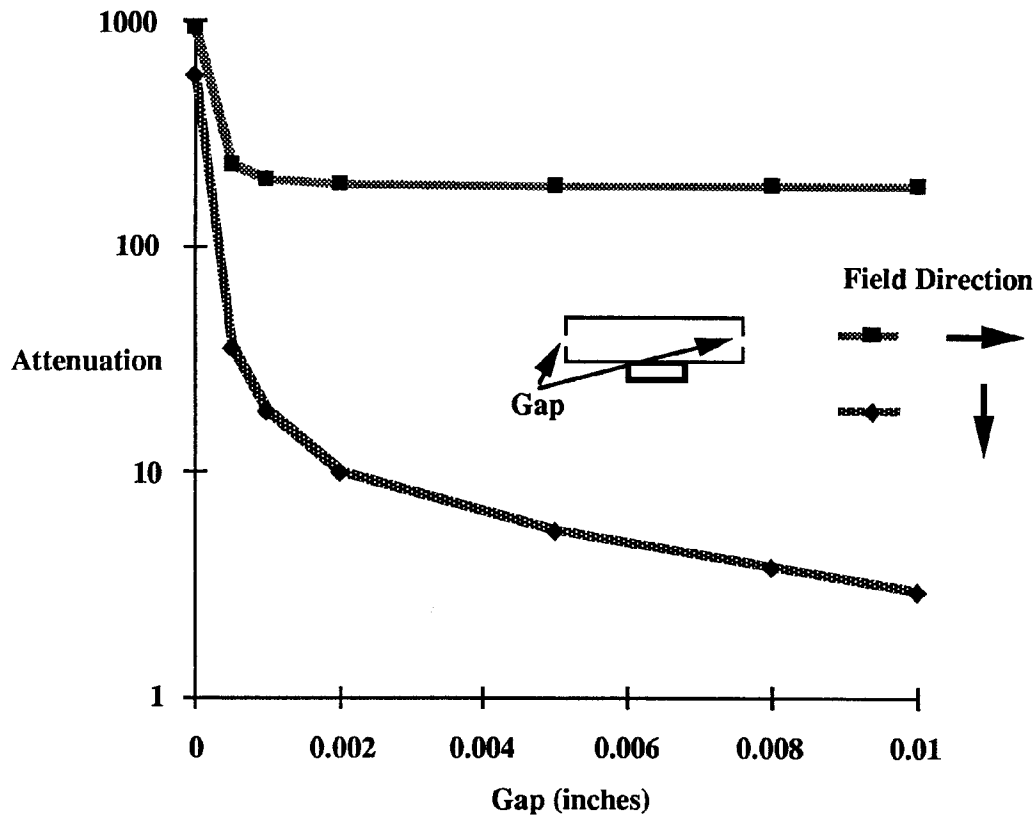


Figure 3 Attenuation vs. gap for the two magnetic field orientations.

## Use of Superconductors for Accelerometers

### *Problem Definition*

The most common accelerometer design used today is shown in Figure 4. This spring force method uses a technique whereby a proof mass is hinged from the outside casing of the accelerometer. Under an acceleration the proof mass undergoes a displacement from its rest position. This response follows the dynamics of the spring. The displacement of this proof mass is sensed to determine acceleration. Critical design factors are long-term bias stability and hysteresis associated with the spring constant. Therefore, the stability of the hinge is the key parameter for producing an accelerometer.

The disadvantage of mechanical hinges for high-accuracy accelerometers is feasibility and cost associated with producing the defect- and impurity-free material required for mechanical stability and positional repeatability. Ideally the suspension of a proof mass with electromagnetic fields offers the most predictable and stable hinge technique provided that the proof mass is also stable. Unfortunately, the hysteresis associated with most magnetic proof masses would make it very difficult to design an electromagnetic accelerometer.

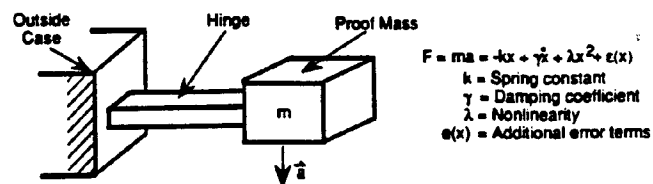


Figure 4 Common accelerometer sensor design and definitions.

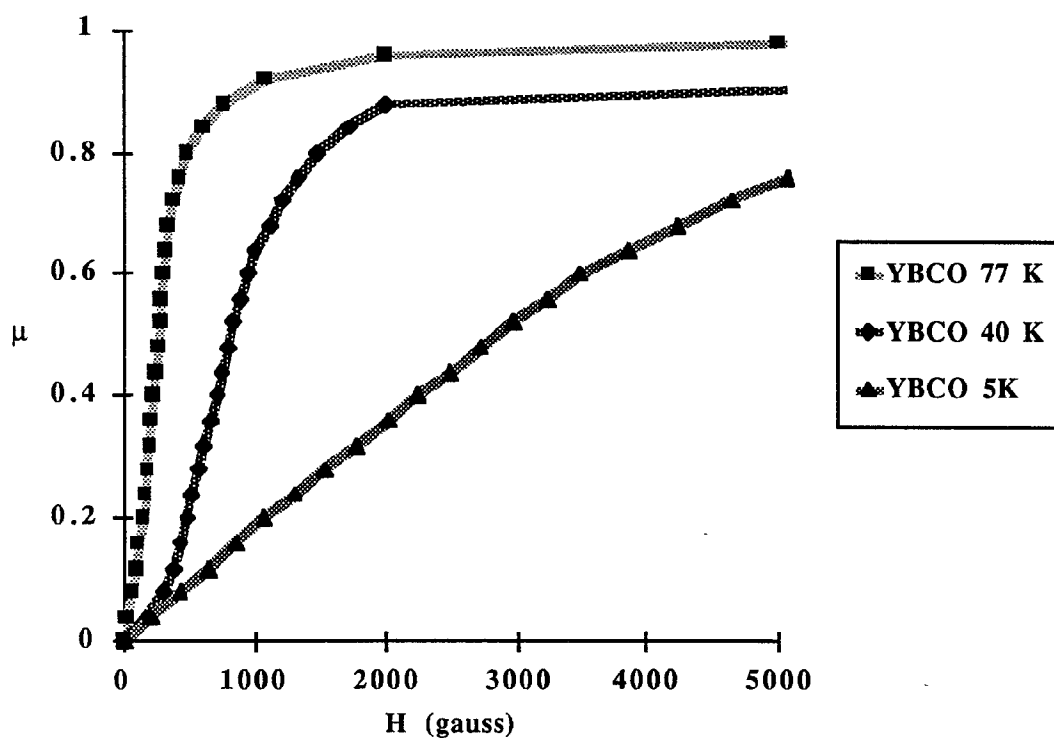


Figure 5 Permeability vs. applied field for 5, 40, and 77 K for the YBaCuO (YBCO) perovskite superconductor.

Use of the Meissner effect in superconductors offers a unique solution to the accelerometer problem. For an ideal superconductor (Type I), a zero  $\mu$  results in a very simple accelerometer design since the material properties are ideally predictable. However, only the perovskites have been found to be superconducting above 77 K (minimum practical operating temperature for an accelerometer), and they are type II superconductors. That is, above a critical field  $H_{c1}$ , they are in a mixed superconducting state whereby  $\mu$  is between 0 and 1. At and above a critical field  $H_{c2}$ , the compounds are no longer superconducting, and thus  $\mu$  is equal to 1. Figure 5 shows the  $\mu$  as a function of applied field for three different temperatures for the YBaCuO superconductor. MSC/EMAS was used to determine the feasibility of using a type II superconductor for accelerometer applications.

### Analysis

Figure 6 shows the two-dimensional finite element model used to determine the forces associated with the Meissner effect for a type-II superconductor.<sup>2</sup> This simple accelerometer design consists of four permanent magnets, with the poles alternating as one circles the model. The back iron decreases the magnetic circuit reluctance. The magnetic field gradient acts to center the diamagnetic superconducting sample, with position sensors used to determine the acceleration.

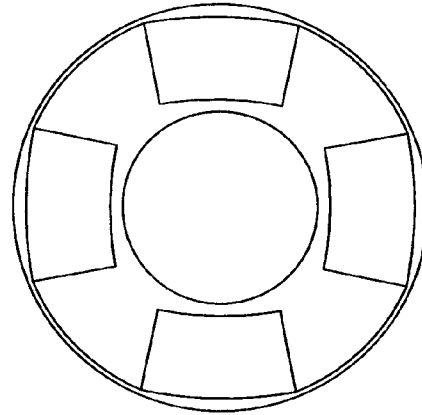


Figure 6 MSC/EMAS model of two-dimensional accelerometer.

The magnetic field lines for this two-dimensional accelerometer are shown in Figures 7 and 8 for the cases of an air core and a superconducting core, respectively. The permanent magnet strength for these two cases was 3000 Gauss. The data for the 77 K YBaCuO sample, as shown in Figure 5, was used to generate the results in Figure 8. The inability of the flux to completely penetrate the YBaCuO sample is clearly evident.

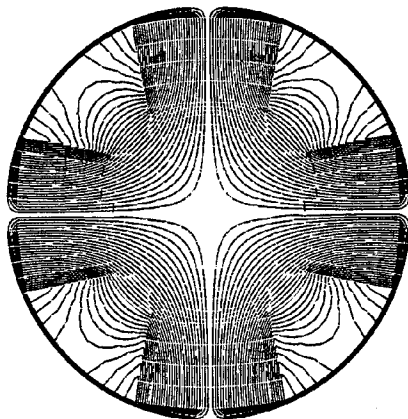


Figure 7 Field line plots for air core and 3000 Gauss permanent magnets.

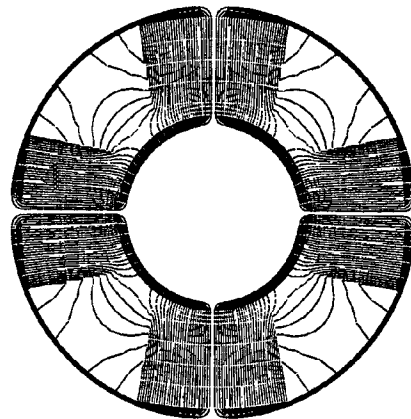
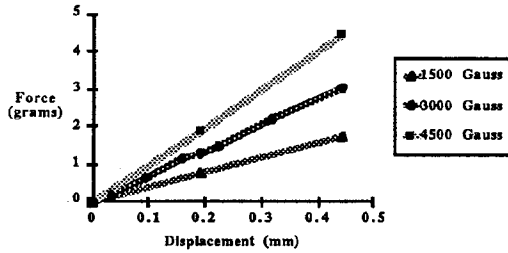


Figure 8 Field line plots for superconducting core (YBaCuO at 77 K) and 3000 Gauss permanent magnets.

The force due to the Meissner effect was calculated by comparing the Total Magnetic Co-Energy of two different MSC/EMAS runs, with the superconductor slightly displaced from center in one of the runs. The force is determined from the equation (Ref. 3)

$$\text{Force} = [(\text{Co-Energy2}) - (\text{Co-Energy1})] / \text{Displacement} \quad (1)$$

Figure 9 shows force vs. displacement data for three different permanent magnet field strengths for YBaCuO at 77 K. As expected, these curves show a near linear relationship. The curves also show a diminishing relative force for higher field strengths. This effect is due to the higher  $\mu$  for higher field strengths, thus resulting in lower relative forces.



**Figure 9** Comparison of the forces generated by YBaCuO at 77K for three different permanent magnet field strengths.

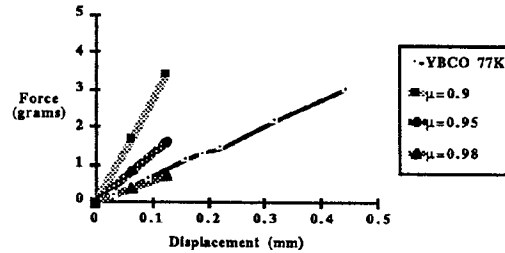


**Figure 10** Comparison of the forces generated by YBCO at 77K and linear diamagnetic materials with  $\mu=0.9$ ,  $0.95$ , and  $0.98$ . The field strength of the permanent magnets was 3000 Gauss.

In Figure 10, the 3000 Gauss data for YBaCuO at 77 K is compared with data from linear materials exhibiting  $\mu$ 's of 0.9, 0.95, and 0.98. The data suggests that for a 3000 Gauss field, the YBaCuO at 77 K produces a force equivalent to that of a linear diamagnetic material with  $\mu=0.97$ . This can be understood by recalling Figure 5.

## Discussions

To implement an accelerometer using superconductors, the superconductor must be constrained in three directions. As a minimum this requires levitating the superconductor against the forces of gravity. From the studies above, it is apparent that relatively large fields are required to generate the necessary levitational forces. As a result, considerable amounts of flux pinning will occur within the superconducting proof mass. This in turn results in hinge friction, or damping. This damping term must be determined to properly calibrate the accelerometer. Therefore, considerable amount of engineering will be needed to construct an accelerometer from the perovskite superconductors, thereby mitigating the potential benefits.

## Proximity Sensor for Aircraft Applications

### Problem Definition

Proximity sensors are commonly made with two coils, one to sense the target and the other to compensate for variations in temperature. This approach requires three wires with one of the wires common to both coils.

For aircraft applications, it is desirable to use only two wires to minimize weight, since each commercial aircraft has over 100 proximity sensors on-board. The use of only two wires allows



for only a single sense coil. With this approach, the DC coil resistance is used to sense temperature, and the real and imaginary impedance of the coil is used to sense target position. The basic two-wire proximity sensor design is shown in Figure 11, along with the equivalent electrical circuit.

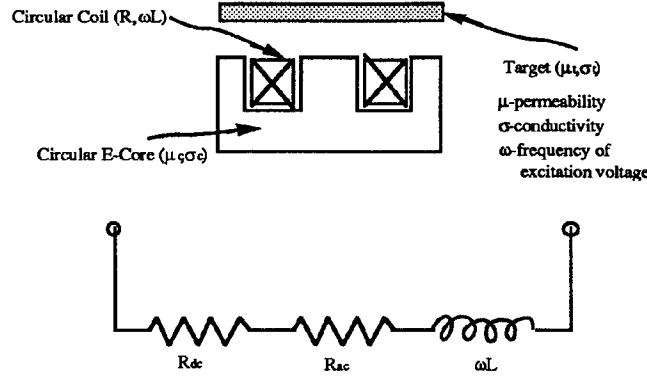


**Figure 11** Sketch of two-wire proximity sensor and sensor definitions.

The problem was to determine the optimum sensor design, and understand the sensor coil impedance as a function of temperature and target position. The design variables include the selection of E-core and target material. To understand the temperature dependance of the sensor, the temperature dependent permeability and conductivity were entered into the MSC/EMAS model.

### Analysis

A simple axis-symmetric finite element model was constructed to analyze the proximity sensor shown in Figure 11. For varying material properties ( $\mu$  and  $\sigma$ ), target position, and coil excitation, the real (eddy current losses) and imaginary (inductance) impedance were determined using the Total Magnetic Energy and Power Loss outputs of MSC/EMAS (Ref. 3). The real impedance ( $R$ ) is equal to

$$R = (\text{Power Loss}) / I_{\text{rms}}^2 \quad (2)$$

and the imaginary impedance ( $\omega L$ ) is equal to

$$\omega L = (\text{Total Magnetic Energy}) / I_{\text{rms}}^2 \quad (3)$$

where  $I_{\text{rms}}$  is the root-mean-square current applied to the coil windings. Figure 12 shows results from the axis-symmetric finite element model for three different types of target materials at six different sensor/target distances. Stainless steel (416) is used as the sensor material ( $\mu=65$  and  $\sigma=1 \times 10^6 \text{ 1}/\Omega\text{m}$ ) due to the highly corrosive environment in which aircraft proximity sensors reside. The three target materials modeled were ferrite ( $\mu=2000$  and  $\sigma=1 \times 10^4 \text{ 1}/\Omega\text{m}$ ), iron ( $\mu=2000$  and  $\sigma=1 \times 10^7 \text{ 1}/\Omega\text{m}$ ), and copper ( $\mu=1$  and  $\sigma=5 \times 10^7 \text{ 1}/\Omega\text{m}$ ). The gaps that separated the sensor and target were infinity and 0.5, 1, 1.5, 2, and 2.5 mm. Equations (2) and (3) were used to determine the real and imaginary coil impedance of the sensor for an excitation frequency of 1 kHz. Significant differences are observed for the three different types of materials.

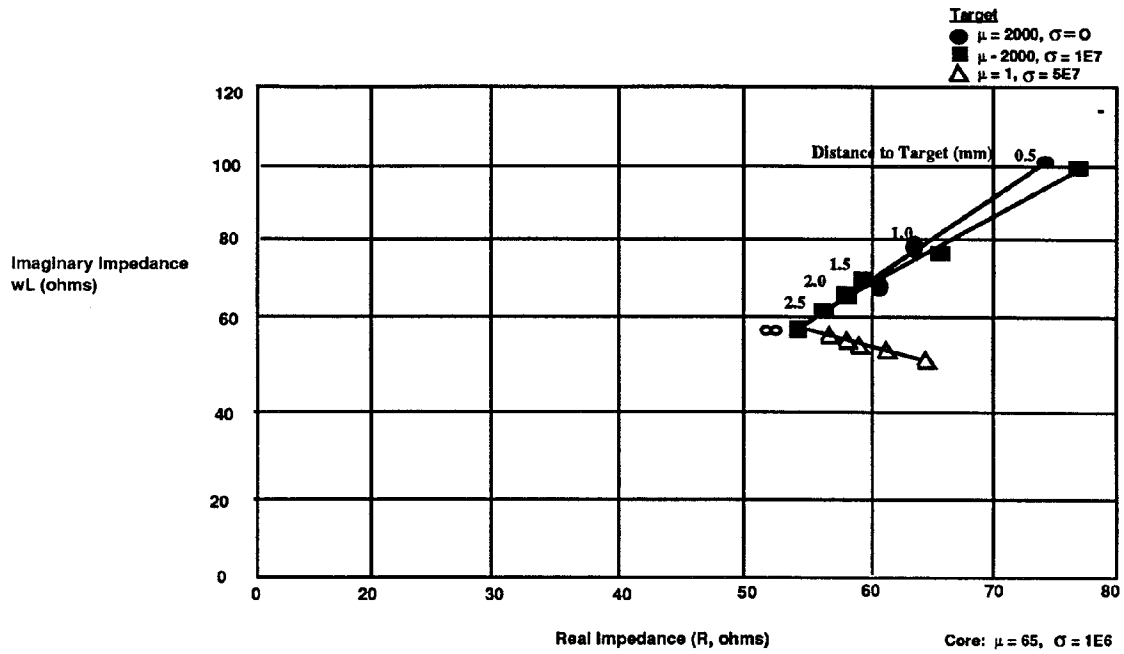


Figure 12 Real and imaginary coil impedance of proximity sensor vs. target position for three different target materials.

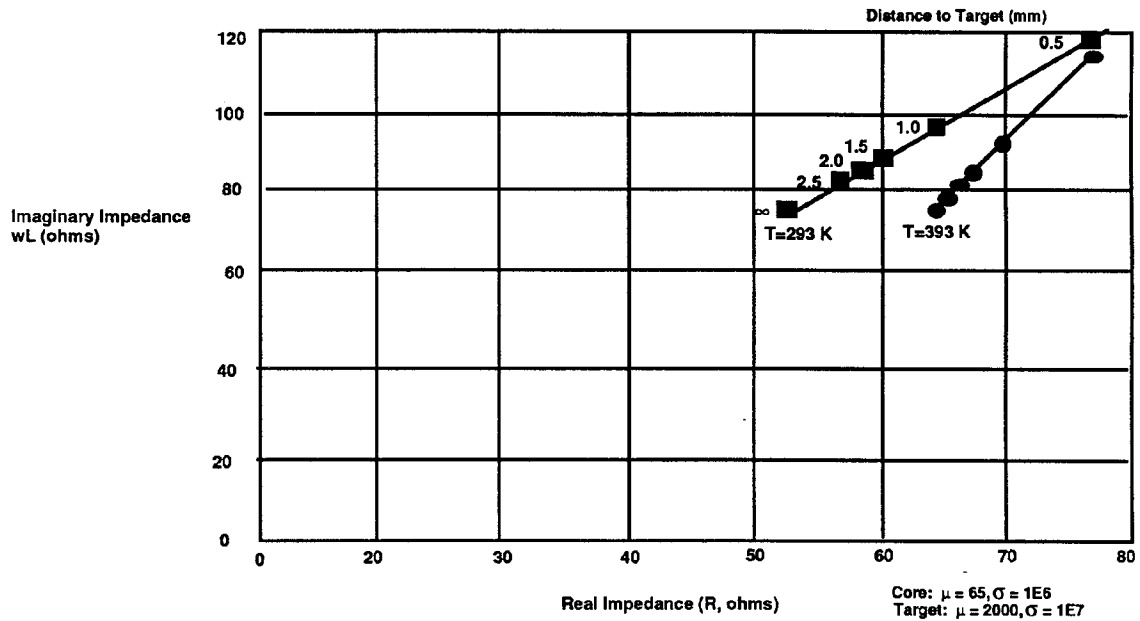


Figure 13 Real and imaginary coil impedance of proximity sensor vs. target position at 293 and 393 K.

Figure 13 shows results from the axis-symmetric finite element model for two different temperatures (293 and 393 K) and six different sensor/target separation distances. Stainless steel (416) was again used as the sensor material and iron was the target material. The temperature variation was modeled using temperature dependent values of  $\mu$  and  $\sigma$ . The distances were the same as those in Figure 12. Again, a 1 kHz coil excitation was modeled. The two curves representing the two different temperatures are significantly different, thus suggesting the need to accurately calibrate the DC coil resistance (temperature) with the real and imaginary coil impedance.

### Discussions

A two-wire proximity sensor prototype was designed and built based on the finite element analysis. The modeling was used to optimize the sensor sensitivity to target location while minimizing its sensitivity to temperature. A special electronic circuit, Proximity Sensor Electronics Unit (PSEU), was designed and constructed to measure the DC coil resistance (to get sensor temperature) and the AC coil impedance (to determine target position). The DC resistance was measured by running a DC current through the coil and measuring the DC voltage drop. The AC resistance was measured by driving the coil sinusoidal with a current pump and recovering the amplitude of the in-phase and out-of-phase impedance components using standard phase sensitive detection techniques.

A comparison of the finite element results and the experimental results from the prototype sensor are shown in Figure 14. The data plotted in Figure 14 was obtained at room temperature. Excellent agreement was found for the MSC/EMAS results and the prototype sensor results.

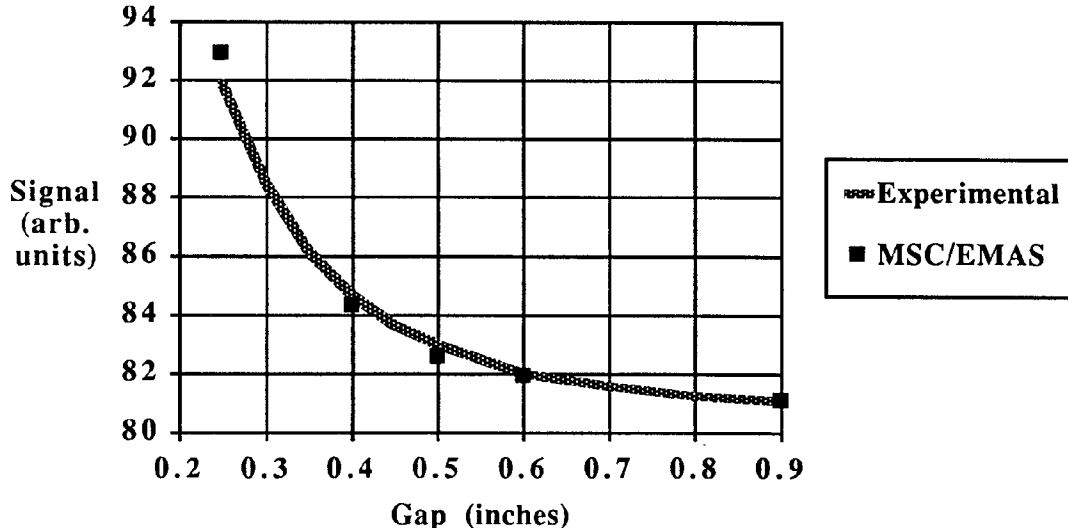


Figure 14 Comparison of experimental and MSC/EMAS results for prototype proximity sensor vs. gap between sensor and target.

## Position Sensor for Aircraft Applications

### *Problem Definition*

Modern aircraft are designed for fuel efficiency at cruising altitudes, and thus have leading edge slats to improve wing performance during take-offs and landings. The position of these slats have become flight critical, and thus it is necessary to know their position at all times. The total travel is several inches, so existing proximity sensors (discuss above) are not applicable. It is desired to have an absolute measuring system, such that the position is unambiguously known even after a power outage. This rules out a target "counting" system. LDVTs would provide the necessary position information, but contain water traps that are undesirable for this hostile environment. Therefore, there is a need for an absolute slide-by position sensor, one that contains no water traps, and can sense targets up to an inch away.

### *Analysis*

Several sensor designs were considered, with the two most promising designs modeled using MSC/EMAS. Of these two designs, finite element analysis showed the most encouraging results for the position sensor shown in Figure 15. This sensor unit consists of two U-shaped cores, one that senses the presence of a wedge shaped target and the other a rectangular target. The wedge-shaped target is the position indicator, while the rectangular target acts as a reference and is used to remove gap and temperature dependencies. Unlike proximity sensors (discussed above) that have a single degree of freedom to be sensed (i.e. gap), the two degrees of freedom needed for position sensing (i.e. gap and horizontal position) necessitates the use of a reference target.

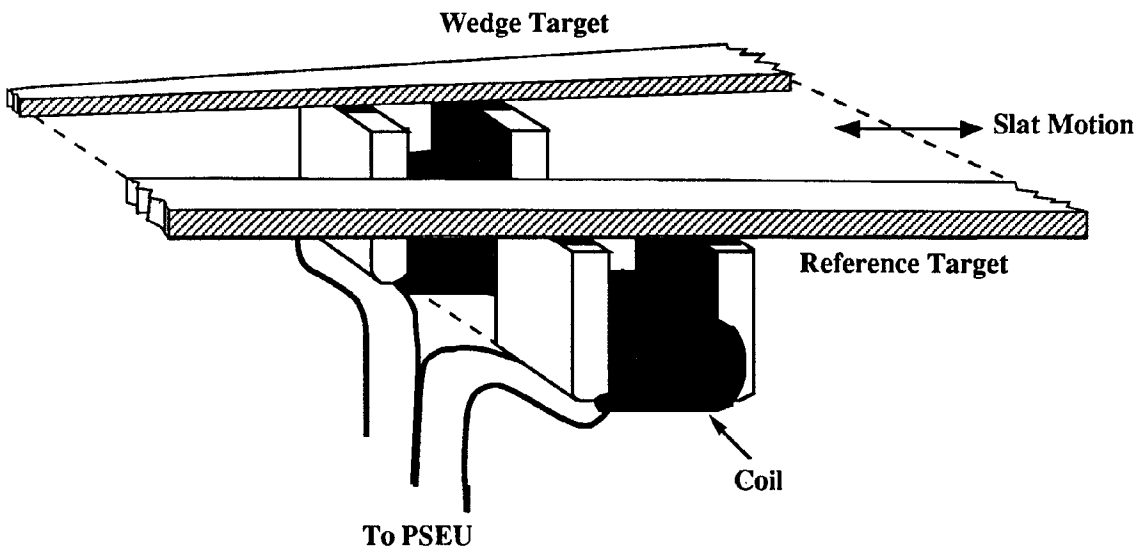


Figure 15 Sketch of position sensor.

In addition to aiding in the sensor selection, finite element analysis was also used to determine design specifics like core material, target material, and target shape. Optimum performance was obtained for laminated U-cores and an iron target. The U-cores were laminated to minimize eddy current losses within the core. The targets were made of iron and thus have a high permeability and electrical conductivity. This combination of U-cores and targets provided the largest modeled variation in eddy current losses as a function of target material cross-section according to the finite element analysis.

The shape of the wedge target was determined from three-dimensional finite element analysis using MSC/EMAS. Figure 16 shows a plot of power loss (eddy current losses or in-phase impedance) and inductance (out-of-phase impedance) vs. wedge target position (inches) for an iron target. The analysis shows a much larger variation for the in-phase impedance. Since the sensor casing (316 stainless steel) was also modeled, the power loss does not go to zero for the no target condition. The analysis shows a nearly linear power loss vs. wedge target position relationship, with non-linear effects occurring while the wedge target width goes to zero. This nonlinearity can be attributed to fringing field effects, and thus the final wedge target design avoided this region.

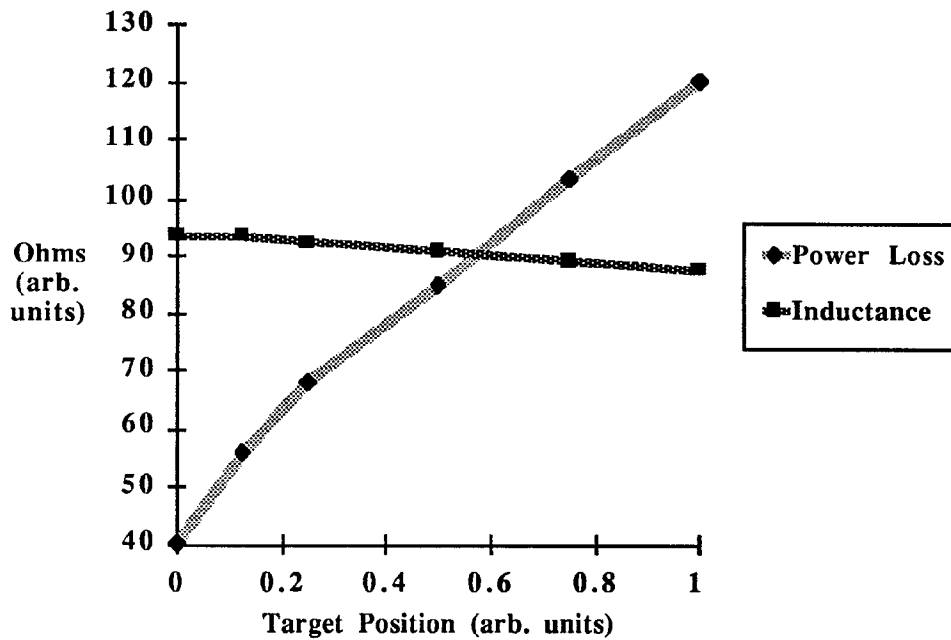


Figure 16 Theoretical analysis of the position sensor using MSC/EMAS. The analysis was conducted for a target/sensor gap of 0.25".

### Discussion

A single-pass sensor prototype was built based on the above finite element analysis. Figure 17 shows experimental sensor output (eddy current loss) vs. target position data obtained from this prototype. The coil was situated inside the 316 stainless steel housing while these tests were conducted. The wedge target width was 0.2 inches at one end and 1 inch at the other end. The total length was 16 inches. The output signal was obtained using the PSEU card discussed above. Data was obtained for gaps of 0.25 (filled squares), 0.5 (open squares), and 0.75 inches (triangles). As predicted by MSC/EMAS, the eddy current losses are a linear function of target position provided that small wedge widths ( $<0.2$ " ) are avoided. Analysis of several sets of data suggest that the overall position resolution of this sensor was better than  $\pm 0.25$ " for a gap of 0.25",  $\pm 0.375$ " for a gap of 0.5", and  $\pm 0.5$ " for a gap of 0.75".

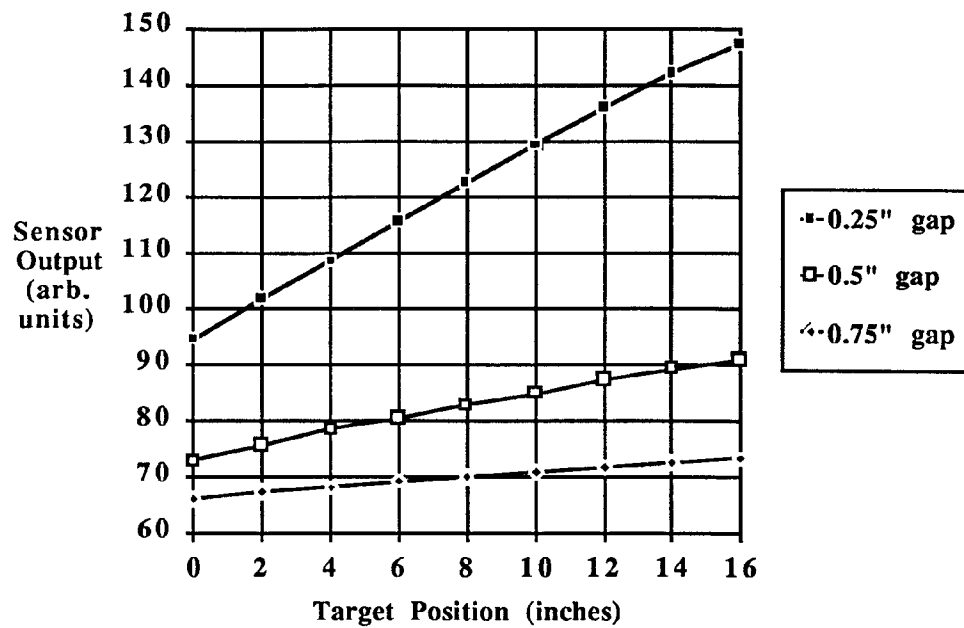


Figure 17 Experimental results from position sensor prototype.

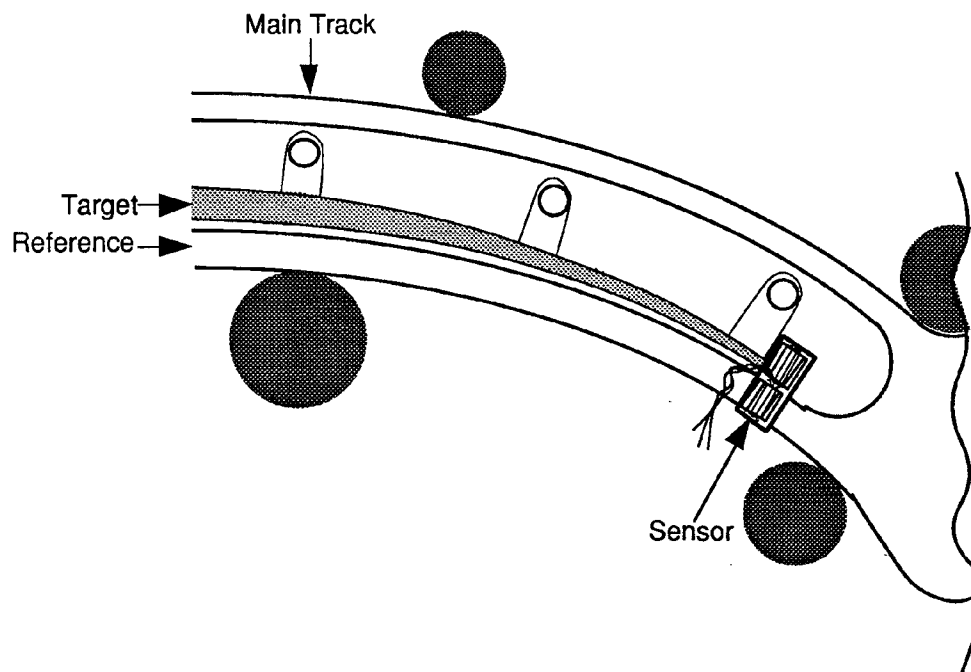


Figure 18 Position sensor layout for leading-edge slat application.

Figure 18 shows a sketch of the implemented sensor. The reference is provided by a structure member that has constant width throughout the 16 inches of travel. The single piece wedged-shaped target is molded to fit the contour of the slat assembly.

## Magnetic Bearings and Actuators

### *Problem Definition*

Existing mechanical bearings and actuators have reduced lifetimes. The use of electromagnetic bearings and actuators are expected to significantly increase these lifetimes. However, the size, weight, and power requirements will depend critically on the magnetic bearing and actuator design.

A two-dimensional sketch of a magnetic actuator is shown in Figure 19. The rotor is spinning at 12000 revolutions per minute (RPM). The purpose of this modeling effort was to determine the power losses (drag torque) in the rotor due to its spinning motion. This homo-polar geometry minimizes core losses since only a portion of the B-H loop is traversed for any given rotor element. The rotor consists of two main parts, the maraging steel support structure and the hyperco50 laminations. The stators are made from hyperco50 laminations.

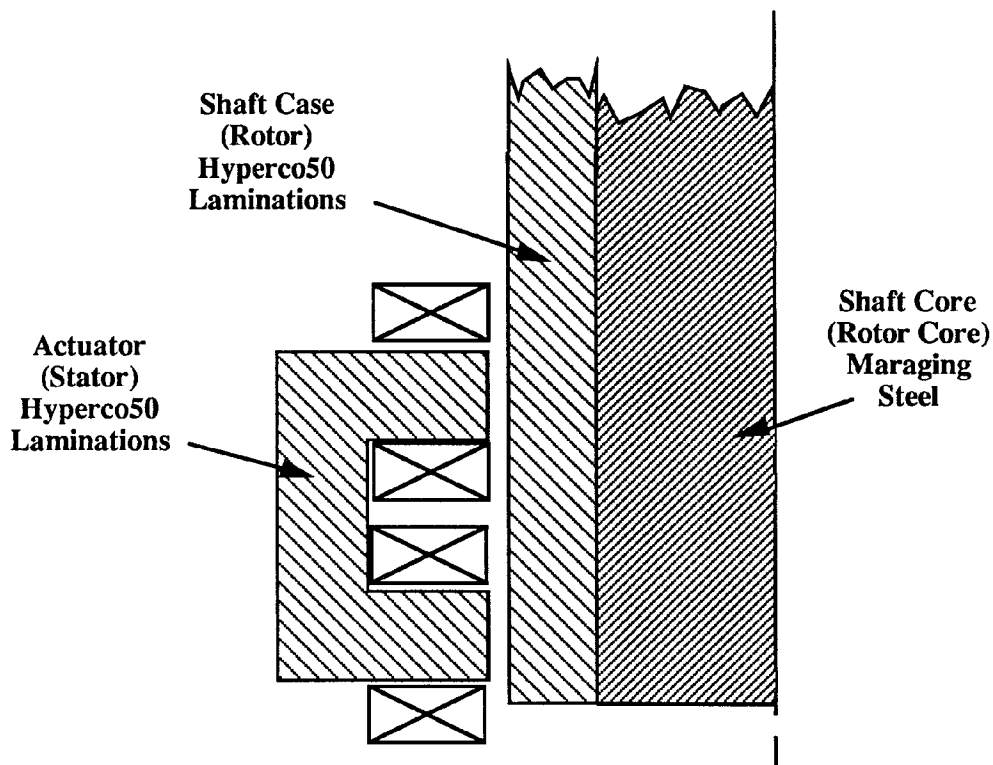


Figure 19 Two-dimensional sketch of the magnetic actuator.

### *Analysis*

Both the hysteresis and eddy current losses were estimated for the actuator shown in Figure 19. The hysteresis losses were estimated using manufacturer loss data for hyperco50 and maraging

steel and two-dimensional field plots obtained using MSC/EMAS. Since the stators are oriented such that the fields within the rotor never change directions, the hysteresis losses will be significantly less than those published for a full B-H loop. For this study, it was assumed that the losses encountered will be  $\sim 1/3$  of those expected if one were to transverse the full B-H loop. The total hysteresis losses were estimated to be in the 10's of watts, thus negligible compared to the eddy current losses.

The eddy current losses were estimated using nonlinear transient response analysis. As a portion of the rotor moves by the stator pole, it experiences a magnetic flux density which rises abruptly from zero to some maximum value, remains at that value for an extended period, and then falls abruptly to zero again. This will take place twice during each rotor cycle. The spatial profile of the stator fringing field was determined; the resulting flux density profile is shown in Figure 20. From the outer radius of the rotor (5.4") and the rotor rotation rate (12,000 RPM), the spatial profile was converted into the time profile shown in Figure 20. As shown in Figure 20, the steepest portion of this time profile is well fitted by a 11 kHz sine wave.

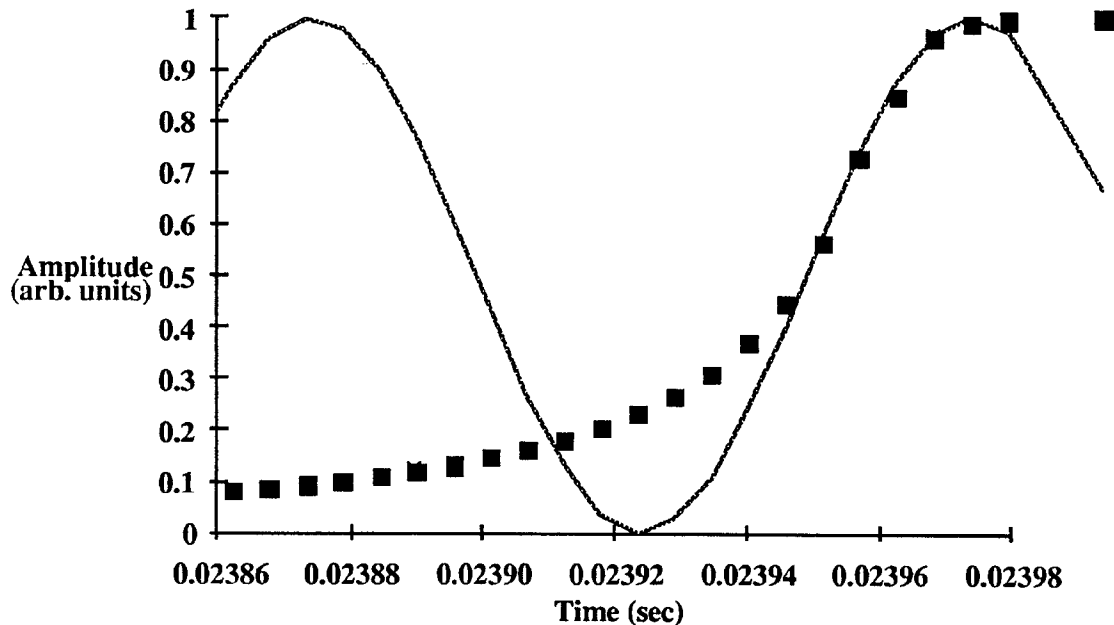


**Figure 20** Fringing magnetic field of the actuator stator as seen from the rotor reference frame. The fringing field is fitted to a 11 kHz sine wave.

A two dimensional finite element model of the actuator shown in Figure 19 was used to determine the losses in the maraging steel. The conductivity in the hyperco50 laminations was assumed to be zero. The eddy current losses predicted by the nonlinear transient response analysis are shown in Figure 21 as a function of time. Also shown in Figure 21 is the transient response curve. The total power loss was determined by integrating the power loss for the full cycle, and multiplying this by 400 edges per second (200 RPS  $\times$  2 actuators) and by the circumference of the rotor (since all rotor material will experience these losses). The result is in good agreement with that found for frequency response analysis using a 11 kHz sine curve, divided by the appropriate duty cycle. The result was about 1000 watts, which can then be converted into a drag torque. This value is significantly larger than the losses found from hysteresis effects.



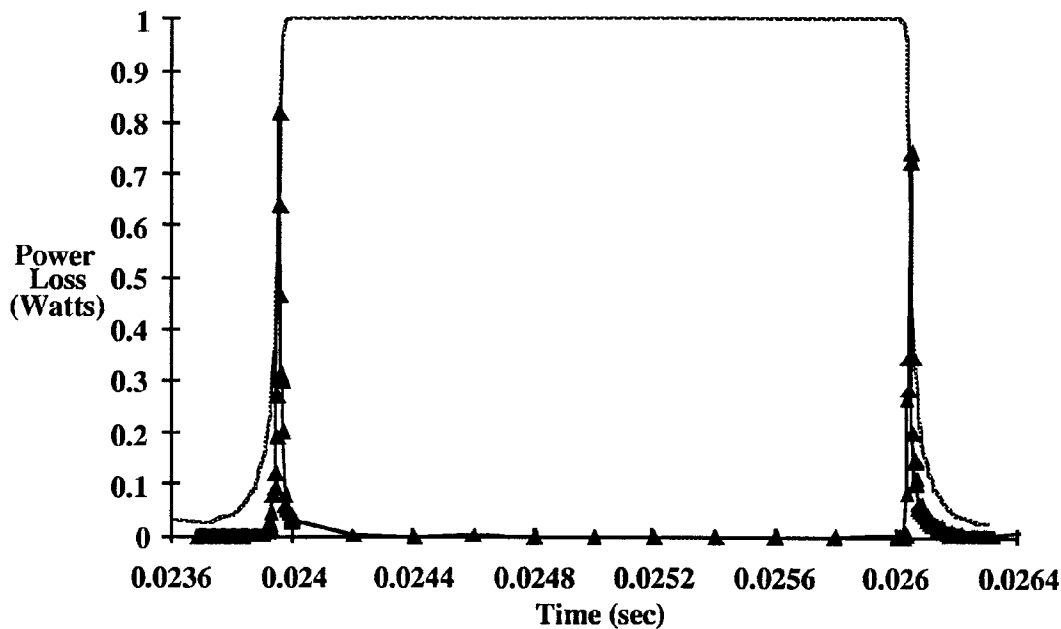


Figure 21 Power loss in the maraging steel vs. time for a complete transient response analysis cycle.

### Discussions

This particular study shows the reduction of a complicated three-dimensional model with moving parts into a series of relatively simple two-dimensional models. A two-dimensional model was used to determine the fringing fields, which was converted into a transient response function, that was subsequently inputted into the original two-dimensional model. The result was an estimation of the eddy current losses in the rotor. In addition, the two-dimensional field plots were used in conjunction with manufacturer core-loss data to determine the hysteresis losses within the rotor.

### Conclusions

The above examples represent the diversity of finite element analysis encountered by the research and development scientist. For many applications, simple two-dimensional analysis allows for sufficient understanding of the problem. In cases where symmetry does not allow for two-dimensional analysis, three-dimensional analysis has proven to be very valuable, but at a cost. The increased time spent in running the finite element model and pre- and post-processing still lends itself to avoid three-dimensional modeling whenever possible. However, advances in computer processing power has continued to narrow this gap between the time associated with two and three dimensional modeling.

The examples discussed above make use of the many different analysis types offered by MSC/EMAS. In addition, they demonstrate the use of Total Magnetic Energy to determine coil inductance, Power Loss to determine eddy current losses, and Total Magnetic Co-Energy to determine force. The use of MSC/EMAS and these relationships have proven to be very reliable at predicting sensor performance.

## Acknowledgements

The authors wish to thank Dr. John Brauer and Mr. Chuck Figer for many helpful discussions.

## References

- [1] Chen, Q.Y., McArdle, J.L., Werner, T.R., and Lenz, J.E., "Magnetic Shielding Properties of YBa<sub>2</sub>Cu<sub>3</sub>O<sub>7-x</sub> Superconductors," Appl. Phys. Lett., Vol. 57, 1990, pp. 2603-2605.
- [2] Torng, Terry, Chen, Quark, Morton, Blaise, and Lenz, Jim, "Hysteretic Magnetic Forces Calculation for Type-II Superconductors," IEEE Transactions on Magnetics, Vol. 28, 1992, pp. 2229-2231.
- [3] Brauer, John R., *What every engineer should know about finite element analysis*, Chapter 5, Marcel Dekker, Inc., 1988.